Progress In Electromagnetics Research B, Vol. 118, 119–134, 2026

PIER B

(Received 9 June 2026, Accepted 13 August 2026, Scheduled 9 September 2026)

A Novel Flux-Linkage-Based Virtual Synchronous Generator with Low-Ripple Active-Power Feedback for Grid-Forming Converters

Yuexi Yang[1], Ziwei Zhao[1], Sichao Wang[1], Fangyuan Li[1], Liwen Zheng[1], and Yang Liu[2,*]

[1]*State Key Laboratory of Advanced Power Transmission Technology (China Electric Power Research Institute Co. Ltd.) Beijing 102209, China*
[2]*School of Electric Power Engineering, South China University of Technology, Guangzhou 510640, China*

ABSTRACT: Virtual synchronous generator (VSG) control is a representative grid-forming strategy for converter-interfaced renewable generation. In a conventional VSG, active-power feedback is calculated directly from terminal voltage and current, allowing voltage distortion and weak-grid-induced oscillatory components to enter the swing loop. This paper proposes a flux-linkage-based active-power calculation that reconstructs electromagnetic flux linkage from the measured converter voltage and evaluates active power through the flux-current relation. The calculation is integrated into a VSG controller with cascaded voltage and current inner loops. A small-signal impedance model and PSCAD/EMTDC simulations are combined to characterize the feedback-interaction mechanism and validate the method under grid-impedance, operating-point, disturbance, and filter-parameter variations. Compared with the conventional voltage-based VSG, the proposed method reduces steady-state active-power peak-to-peak ripple by 56.7–65.8% and frequency ripple by 42.6–66.7% in the grid-impedance sweep, and reduces the non-dc active-power component by 69.9–72.7% across the tested operating points, while maintaining comparable terminal current and voltage THD. Closed-loop active-power-command tests further quantify the associated reactive-power and local terminal-voltage responses under three converter-grid interface conditions. The impedance model identifies a 37.3% lower normalized resonance peak in the 40–250 Hz interaction band, while an electromagnetic transient (EMT) spectral study sampled at 50 kHz characterizes the adjacent 10–40 Hz and 500 Hz–10 kHz bands. These results demonstrate that flux-linkage-based power feedback improves the quality of the signal driving the virtual swing equation within a practical VSG architecture.

1. INTRODUCTION

Grid-forming converters are becoming a key interface for wind power, photovoltaic generation, and energy-storage stations in low-inertia power systems. International studies have converged on the same basic need: converter stations should no longer behave only as grid-following current sources, but should actively establish voltage, frequency, and damping support in weak or converter-dominated grids [1, 2]. This requirement has led to several grid-forming control families, including droop control, power-synchronization control, match control or capacitor-voltage synchronizing control, virtual synchronous generator (VSG)/synchronverter control, and virtual oscillator control.

Direct-drive permanent-magnet synchronous generators are a representative machine-side option for low-speed wind turbines [3]. Such turbines use a full-scale power converter to interface the generator with the ac grid. The proposed flux-linkage-based VSG can be used in the grid-side converter to provide grid-forming voltage and frequency regulation.

Droop control is the earliest and most widely deployed grid-forming method in microgrids. It regulates frequency and voltage magnitude according to active- and reactive-power deviations, so multiple converters can share load without high-bandwidth communication [4, 5]. Its main advantages are structural simplicity and engineering maturity. However, conventional droop control has no explicit inertia state, produces steady-state frequency and voltage deviations, and is sensitive to line impedance and P-Q coupling. In weak grids, its low-frequency damping and transient performance depend strongly on virtual impedance and secondary control design.

Power-synchronization control (PSC) was proposed to operate voltage-source converters without a phase-locked loop under very weak grid conditions [6]. PSC synchronizes the converter by using the active-power/phase-angle relation, which gives it a physical similarity to synchronous-machine power-angle dynamics. This makes PSC attractive for high-voltage direct-current and renewable converter stations connected to weak grids. Nevertheless, PSC requires careful damping design, current limitation, and transition handling during grid faults. Since the synchronization variable is still driven by measured active power, power ripple and distortion may also affect its dynamic behavior.

Match control, also reported as capacitor-voltage synchronizing control in Type-4 wind-turbine-generator applications, establishes grid-forming operation via the converter capacitor-voltage vector rather than via a phase-locked loop (PLL)-based grid angle [7]. By making the controlled capacitor voltage

* Corresponding author: Yang Liu (epyangliu@scut.edu.cn).

doi:10.2528/PIERB26060906

TABLE 1. Comparison of representative grid-forming control methods and the positioning of this work.

Method	Basic principle	Main advantages	Main limitations related to this study
Droop control	Adjusts frequency and voltage magnitude according to active/reactive power errors.	Simple, communication-free, mature in microgrid applications.	No explicit inertia; steady-state deviations; sensitive to line impedance and P-Q coupling.
Power-synchronization control	Uses active-power/angle dynamics to synchronize a voltage-source converter without PLL.	Suitable for very weak grids; simple synchronization structure.	Damping, current limitation, and fault transition need careful design; measured-power ripple can enter the synchronization loop.
Match control/ capacitor-voltage synchronizing control	Uses the controlled converter capacitor-voltage vector as the synchronizing voltage source for grid-forming operation.	Can provide inertial and primary frequency responses without relying on a PLL angle.	Performance depends on capacitor-voltage loop design, inner-loop bandwidth, and current limitation; feedback ripple still requires damping treatment.
VSG/synchronverter	Emulates swing and excitation equations of synchronous machines.	Explicit inertia and damping; intuitive for grid-support design and large renewable stations.	Conventional voltage-current power calculation injects ripple into the swing equation under distorted or weak-grid conditions.
VOC/dVOC	Uses nonlinear oscillator dynamics to generate and synchronize converter voltage waveforms.	Decentralized synchronization and fast response.	Parameter design, current limiting, and large-station engineering integration are less mature.
This work	Keeps the VSG and inner-loop framework, but replaces direct voltage-based power feedback with flux-linkage-based active-power calculation.	Reduces non-dc active-power feedback and frequency ripple while retaining a practical VSG architecture.	Performance depends on estimator bandwidth, controller tuning, filter parameters, and coordinated current limiting.

behave as the synchronizing voltage source, this method can provide inertial and primary frequency responses for full-scale wind turbines. Its advantage is that the grid-forming voltage is directly tied to the converter ac-side energy storage element, which is physically meaningful for wind-power converters. However, the synchronization and inertial response depend on the capacitor-voltage control loop, the inner-loop bandwidth, and the coupling with current limitation. Under distorted voltage or weak-grid conditions, power and voltage feedback paths still require careful filtering and damping design.

VSG and synchronverter controls emulate swing and excitation equations of synchronous machines and are therefore intuitive for inertia and damping design [8–11]. Compared with droop control, VSG introduces explicit virtual inertia and damping, which helps renewable converters provide grid-support behavior similar to synchronous generators. For this reason, many studies have focused on VSG parameter tuning, weak-grid stability, current limitation, fault ride-through, and impedance interactions. However, the VSG swing equation is directly driven by the calculated active power. In most implementations, instantaneous active and reactive powers are calculated from measured terminal voltage and current. Under voltage distortion, weak-grid impedance, or grid faults, this direct voltage-current multiplication introduces oscillatory components into the active-power feedback, and the resulting ripple acts as a disturbance torque in the virtual swing equation.

Recent studies confirm that the choice of electrical-power feedback variable can change the small-signal behavior of a grid-forming VSG. For example, Zhou et al. compared actual-current and virtual-current power calculations in a dual-loop VSG [12], while virtual-admittance control provides another weak-grid grid-forming architecture with experimentally demonstrated fault and islanding operation [13]. In this paper, we retain the measured filter-current feedback, while replacing the terminal-voltage factor with a mean-removed flux linkage. As summarized in Table 1, this design conditions the active-power feedback entering the swing loop within a conventional cascaded VSG architecture.

Virtual oscillator control (VOC) and dispatchable VOC synchronize converters via nonlinear oscillator dynamics rather than an explicit power-angle or swing equation [14, 15]. VOC has attractive decentralized synchronization properties and fast dynamic response. It is promising for inverter-dominated microgrids, but its parameter design, current limiting, protection coordination, and extension to large wind-power stations remain less mature than VSG-based implementations. Therefore, VSG remains a practical and understandable framework for large renewable converters, provided that its feedback-signal quality and weak-grid interaction dynamics are properly addressed.

Table 1 compares representative grid-forming methods. These methods differ mainly in their synchronization mechanisms, but many still rely on measured active power or power-angle dynamics. For VSG-controlled wind-turbine converters, a less emphasized but direct problem is therefore the quality of the active-power feedback signal itself. If the calculated active power contains oscillatory components, the virtual inertia and damping loop transfers part of this

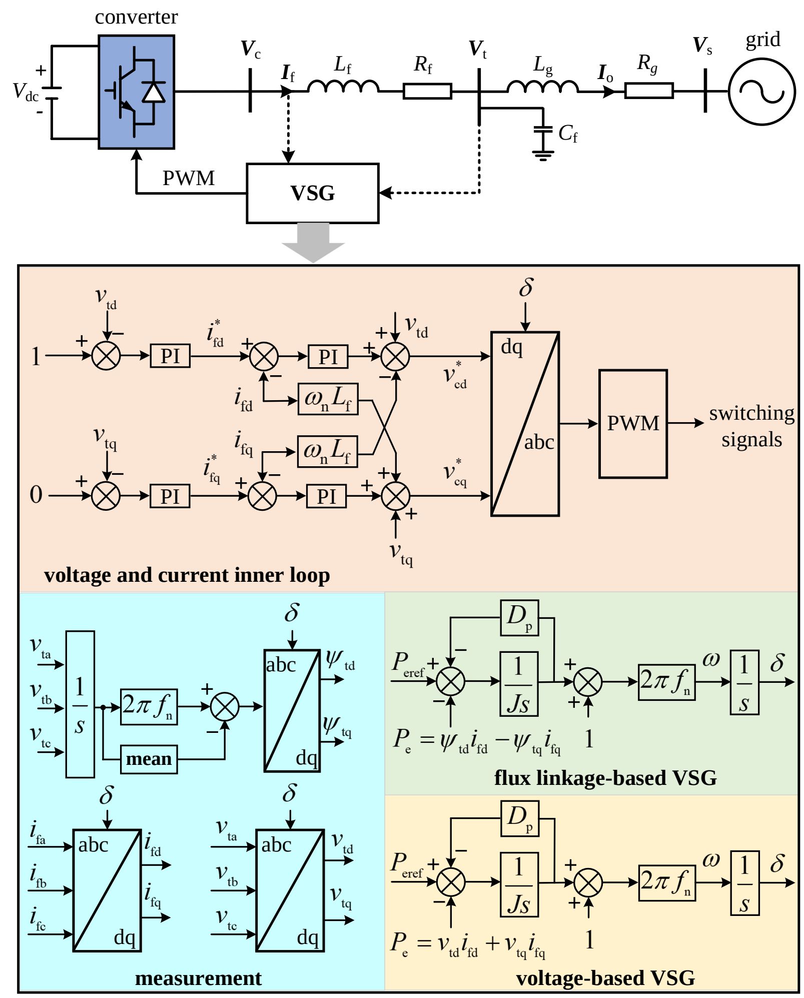

FIGURE 1. Control block diagrams of the flux-linkage-based and voltage-based VSGs with identical cascaded voltage and current inner loops.

disturbance into frequency and angle oscillations. This paper investigates a flux-linkage-based active-power calculation method to address this issue within the VSG framework. The core idea is to reconstruct the electromagnetic flux linkage from terminal voltage and current and then calculate active power from the flux-current relation. Compared with direct voltage-current multiplication, the flux-linkage path conditions the active-power signal before it enters the swing loop; the analysis below identifies its principal method-dependent attenuation in the 40–250 Hz synchronization-interaction band.

The contributions are as follows. First, a mean-removed flux-linkage estimator is incorporated into the active-power feedback of a cascaded VSG while retaining the established voltage and current inner loops. Second, a small-signal output-impedance model is derived to reveal how the power-calculation path modifies the converter-grid interaction, with particular attention to the 40–250 Hz synchronization band. Third, automated PSCAD/EMTDC studies quantify active-power ripple, non-dc power content, frequency response, and terminal total harmonic distortion (THD) under variations in grid impedance, operating point, filter parameters, and disturbance type. Fourth, dedicated closed-loop studies characterize active-reactive power coupling under active-power commands and provide frequency-resolved evidence in the 10–40 Hz and 500 Hz–10 kHz bands.

The remainder of this paper is organized as follows. Section 2 presents the system configuration and cascaded VSG controller. Section 3 derives the flux-linkage-based active-power calculation. Section 4 develops the small-signal and impedance model. Section 5 discusses the numerical simulation results, and Section 6 gives the conclusion.

2. SYSTEM AND CONTROL STRUCTURE

Figure 1 shows the control structures of the studied grid-forming converter. The outer VSG loop generates the internal angle δ in rad, angular frequency ω in rad/s, and voltage magnitude command from active/reactive power references. The voltage reference is then tracked by a cascaded voltage-current inner-loop controller. The flux-based and voltage-based models use the same converter bridge, filter, grid circuit, voltage PI loop, and current PI loop; the only intended difference is the power-feedback calculation.

The VSG swing equation is

$$J\frac{d\omega}{dt} = \omega_0[P_{\text{eref}} - P_{\text{e}} - D(\omega - \omega_0)/\omega_0], \tag{1}$$

TABLE 2. Controlled steady-state P-Q coupling example from (6). The grid-impedance magnitude is fixed at $|Z_g| = 0.20$ p.u.; E and δ are selected in every row to maintain the same initial point, $V = 1$ p.u., $P = 0.60$ p.u., and $Q = 0$.

R/X	ΔP for $\Delta E = 0.05$	ΔQ for $\Delta E = 0.05$	ΔP for $\Delta\delta = 2^\circ$	ΔQ for $\Delta\delta = 2^\circ$
0.0	0.0302	0.2607	0.1716	0.0239
0.1	0.0561	0.2624	0.1752	0.0065
0.5	0.1512	0.2451	0.1719	-0.0615
1.0	0.2269	0.1990	0.1449	-0.1194

where J is the virtual inertia in $\mathrm{kg \cdot m^2}$; D is the damping coefficient; P_{eref} is the reference active power in p.u.; P_{e} is the calculated electrical power in p.u.; and ω_0 denotes the rated angular frequency in rad/s. The voltage command in the synchronous frame can be written as

$$\mathbf{v}^*_{\text{tdq}} = E^* \begin{bmatrix} 1 & 0 \end{bmatrix}^T, \quad \delta = \int \omega dt. \tag{2}$$

Here, E^* is the reference voltage magnitude in p.u., and $\mathbf{v}^*_{\text{tdq}}$ contains the d- and q-axis voltage references in the dq frame. The inner voltage control loop is designed to track $\mathbf{v}^*_{\text{tdq}}$, and the current reference $\mathbf{i}^*_{\text{fdq}}$ produced by the voltage loop can be written as

$$\mathbf{i}^*_{\text{fdq}} = G_v(s) \left(\mathbf{v}^*_{\text{tdq}} - \mathbf{v}_{\text{tdq}}\right), \quad G_v(s) = K_{pv} + \frac{K_{iv}}{s}, \tag{3}$$

and the inner current loop produces the converter modulation voltage $\mathbf{v}^*_{\text{cdq}}$

$$\mathbf{v}^*_{\text{cdq}} = G_i(s) \left(\mathbf{i}^*_{\text{fdq}} - \mathbf{i}_{\text{fdq}}\right), \quad G_i(s) = K_{pi} + \frac{K_{ii}}{s}. \tag{4}$$

where K_{pv} and K_{iv} are the proportional and integral gains of the inner voltage loop, and K_{pi} and K_{ii} are the proportional and integral gains of the inner current loop. Inner loops determine the fast output-voltage tracking and high-frequency converter output impedance, while the VSG and power-feedback path determine the low-frequency synchronization dynamics.

For the conventional voltage-based calculation in the dq reference frame,

$$P_{\text{e}} = v_{\text{td}} i_{\text{fd}} + v_{\text{tq}} i_{\text{fq}}, \quad Q_{\text{e}} = v_{\text{tq}} i_{\text{fd}} - v_{\text{td}} i_{\text{fq}}. \tag{5}$$

Since P_{e} is a direct input of (1), any ripple in (5) becomes a disturbance to the frequency loop. The proposed model keeps the inner loops of (3)–(4) unchanged and replaces only this power-feedback path.

The proposed substitution applies to active-power feedback only; it does not by itself decouple active- and reactive-power loops. For a converter internal voltage $E\angle\delta$ connected to a grid voltage $V\angle 0$ through $R+\mathrm{j}X$, the steady-state transfer relations are

$$\begin{aligned} P &= \frac{R(E^2 - EV\cos\delta) + XEV\sin\delta}{R^2 + X^2}, \\ Q &= \frac{X(E^2 - EV\cos\delta) - REV\sin\delta}{R^2 + X^2}. \end{aligned} \tag{6}$$

Hence, nonzero R/X, operating angle, and voltage excursions introduce cross-couplings among δ, E, P, and Q. The flux-linkage calculation reduces the oscillatory part of P_{e} entering the swing loop, while the Q loop remains the conventional voltage-current calculation. A virtual-impedance or explicit decoupling layer is still needed when the network R/X ratio makes this coupling material [16]. To isolate the effect of R/X from grid strength and operating point, (6) was evaluated with $|Z_g| = 0.20$ p.u., $V = 1$ p.u., and the same initial transfer $P = 0.60$ p.u. and $Q = 0$ in every row. The corresponding E and δ were solved separately for each R/X value. Table 2 gives the finite power changes caused separately by a 0.05 p.u. voltage-magnitude increment and a 2° angle increment. As R/X rises from 0 to 1, the voltage-induced active-power increment grows from 0.0302 to 0.2269 p.u., and the angle-induced reactive-power increment changes from 0.0239 to -0.1194 p.u. This controlled steady-state example establishes the coupling mechanism but is not a dynamic-stability test; the closed-loop EMT validation in Section 5.2 addresses the latter.

3. FLUX-LINKAGE-BASED POWER CALCULATION

The proposed method estimates the converter-side flux linkage as

$$\psi_{\text{ta}} = \int v_{\text{ta}} dt, \quad \psi_{\text{tb}} = \int v_{\text{tb}} dt, \quad \psi_{\text{tc}} = \int v_{\text{tc}} dt, \tag{7}$$

where ψ_{ta}, ψ_{tb}, and ψ_{tc} are estimated node flux linkages. In the synchronous dq reference frame, the electromagnetic torque-like term is

$$T_{\text{e}} = \psi_{\text{td}} i_{\text{fq}} - \psi_{\text{tq}} i_{\text{fd}}, \tag{8}$$

and the corresponding active power is

$$P_{\text{e}} = \omega T_{\text{e}}/\omega_0 \approx T_{\text{e}}. \tag{9}$$

where the assumption $\omega \approx \omega_0$ is used to simplify the power calculation. The proposed method therefore replaces the direct voltage-current multiplication with a flux-current relation.

Fig. 1 highlights the two calculation paths. To reduce the influence of the integration initial condition and slow drift, the node-flux estimator applies moving-mean subtraction to the integrated signal. The voltage-based path reacts immediately to voltage harmonics. The flux-based path introduces a physically meaningful reconstruction of the electromagnetic state. Therefore, high-frequency and low-order oscillatory components in the measured terminal voltage are less likely to appear as active-power feedback ripple.

Estimator robustness: A pure voltage integrator is susceptible to sensor offset, low-frequency noise, and initialization error [17]. The proposed estimator therefore combines a scaled discrete integrator with a ten-sample moving-mean subtraction. For phase $x \in \{a, b, c\}$, it is defined as

$$\begin{aligned} \widetilde{\psi}_x[k] &= \omega \sum_{\ell=0}^{k} v_x[\ell] T_s, \\ \hat{\psi}_x[k] &= \widetilde{\psi}_x[k] - \frac{1}{N}\sum_{r=0}^{N-1} \widetilde{\psi}_x[k-r], \quad N = 10. \end{aligned} \tag{10}$$

Let the measured voltage be $\widetilde{v}_x = v_x + b_x + n_x$, where b_x is a constant bias and $|n_x| \le \bar{n}_x$. The residual flux bias after the moving-mean subtraction is bounded exactly by $|\Delta\hat{\psi}_{x,b}| = \omega T_s (N-1)|b_x|/2$. At a noise angular frequency Ω, the corresponding magnitude bound is

$$|\Delta\hat{\psi}_{x,n}(\mathrm{j}\Omega)| \le \frac{\omega T_s \bar{n}_x}{|1 - e^{-\mathrm{j}\Omega T_s}|} \left| 1 - \frac{1}{N}\sum_{r=0}^{N-1} e^{-\mathrm{j}\Omega r T_s} \right|. \tag{11}$$

Using (8)–(9), a conservative power-error bound is $|\Delta P_\mathrm{e}| \le (\omega/\omega_0)(\|\bar{\mathbf{i}}\|\|\Delta\hat{\boldsymbol{\psi}}\| + \|\bar{\boldsymbol{\psi}}\|\|\Delta\mathbf{i}\| + \|\Delta\hat{\boldsymbol{\psi}}\|\|\Delta\mathbf{i}\|)$. These expressions make the offset/noise sensitivity explicit and show why the mean-removal window and sampling interval must be selected from the sensor specification.

4. SMALL-SIGNAL AND IMPEDANCE ANALYSIS

Small-signal modeling and impedance-based stability analysis are widely used to evaluate converter-grid interactions [11, 18–20]. To explain the stability mechanism, the converter is separated into two coupled parts: the cascaded voltage/current inner loops and the VSG synchronization loop. Around an operating point, the swing dynamics are linearized as

$$\Delta\dot{\delta} \;=\; \Delta\omega, \tag{12}$$

$$J\Delta\dot{\omega} \;=\; \omega_0(\Delta P_\mathrm{eref} - \Delta P_\mathrm{e} - D\Delta\omega/\omega_0). \tag{13}$$

The inner-loop-controlled terminal voltage can be expressed in the small-signal form

$$\Delta\mathbf{v}_\mathrm{t}(s) = G_\mathrm{cl}(s)\Delta\mathbf{v}_\mathrm{t}^*(s) - Z_\mathrm{in}(s)\Delta\mathbf{i}_\mathrm{o}(s), \tag{14}$$

where $G_\mathrm{cl}(s)$ is the closed-loop voltage tracking transfer function; $Z_\mathrm{in}(s)$ is the output impedance shaped by the filter, voltage loop, and current loop; and $\mathbf{i}_\mathrm{o}$ is the grid-side output current. A compact scalar approximation for the dominant channel is

$$\begin{aligned} G_\mathrm{cl}(s) &= \frac{G_v(s)G_i(s)G_\mathrm{pwm}(s)}{1 + G_v(s)G_i(s)G_\mathrm{pwm}(s)}, \\ Z_\mathrm{in}(s) &= \frac{Z_f(s)}{1 + G_i(s)G_\mathrm{pwm}(s) + G_v(s)G_i(s)G_\mathrm{pwm}(s)}. \end{aligned} \tag{15}$$

where $G_\mathrm{pwm}(s)$ denotes the pulse width modulation (PWM) delay, and $Z_f(s)$ denotes the filter impedance seen from the converter terminal. Eq. (15) shows that the voltage and current inner loops mainly shape the medium- and high-frequency impedance.

The calculated power perturbation that couples the network to the swing loop can be represented as

$$\Delta P_\mathrm{e}(s) = G_p(s)\left(K_\delta\Delta\delta + K_v\Delta v_\mathrm{t} + K_i\Delta i_\mathrm{f}\right), \tag{16}$$

where K_δ, K_v, and K_i are linearized power coefficients associated with angle, terminal voltage, and filter current perturbations, respectively. The factor $G_p(s)$ denotes the normalized oscillatory-power calculation channel after the dc/mean component is removed. For the voltage-based calculation, this channel has a relatively wide bandwidth because the terminal voltage is directly multiplied by current. For the flux-based calculation, the mean-removed flux estimator adds electromagnetic-state reconstruction and attenuation to oscillatory voltage components:

$$\begin{aligned} G_{p,v}(s) &= H_v(s), \\ G_{p,\psi}(s) &= H_v(s)H_\psi(s), \\ H_v(s) &= \frac{1}{1 + sT_v}, \\ H_\psi(s) &= \frac{1}{1 + sT_\psi}. \end{aligned} \tag{17}$$

Eq. (17) is not a replacement of the time-domain flux-linkage calculation in (7)–(9). It is a normalized small-signal representation of the mean-removed oscillatory component that enters the swing loop. The additional factor $H_\psi(s)$ therefore represents the ripple attenuation introduced by flux reconstruction over the studied interaction band.

Combining (14)–(16), the normalized converter output impedance can be written in a compact form as

$$Z_\mathrm{out}(s) = Z_\mathrm{in}(s) + K_z G_\mathrm{cl}(s) G_p(s) G_\mathrm{sw}(s), \tag{18}$$

where K_z is the linearized power-to-voltage coupling coefficient and

$$G_\mathrm{sw}(s) = \frac{\omega_0}{Js^2 + Ds + \omega_0 K_s} \tag{19}$$

is the small-signal swing-loop response from active-power perturbation to the synchronization angle, and $K_s = \partial P_\mathrm{e}/\partial\delta|_0$ is the synchronizing-power coefficient. This expression is consistent with (13), because the rated angular frequency ω_0 scales the per-unit power perturbation in the linearized swing equation. Eq. (18) shows that the inner loops set the basic output impedance, while the active-power calculation path adds a low-frequency synchronization component. A noisier power path produces a larger resonance component in $Z_\mathrm{out}(s)$, while the flux path suppresses the resonance via flux reconstruction.

Fig. 2 and Fig. 3 show normalized output-impedance characteristics. The flux-based path gives a smaller resonance peak in the low-frequency interaction band. The voltage-based path exhibits a larger peak around 112 Hz, consistent with its larger active-power and frequency ripple in EMT simulation. The phase of the flux-based impedance is also more inductive in the same frequency band, which is consistent with a reduced modeled interaction.

Table 3 quantifies the impedance difference shown in Fig. 2 and Fig. 3. In the 40–250 Hz interaction band, the flux-linkage

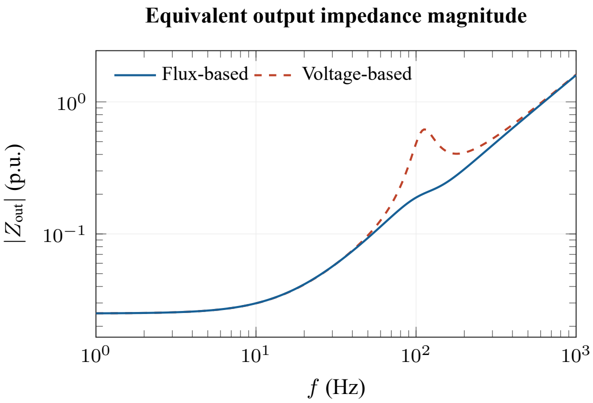

FIGURE 2. Normalized output-impedance magnitude obtained from the linearized equivalent model.

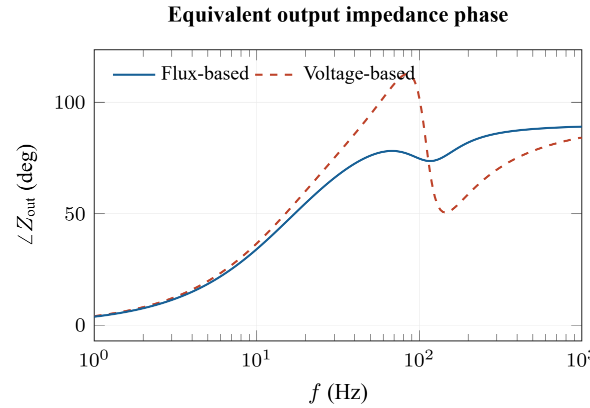

FIGURE 3. Normalized output-impedance phase obtained from the linearized equivalent model.

TABLE 3. Small-signal impedance indicators in the 40–250 Hz band.

Method	Peak $\lvert Z_{\text{out}}\rvert$	Peak freq. (Hz)	Min. phase (deg.)
Flux	0.388	249.9	72.8
Voltage	0.619	112.3	50.6

path reduces the peak normalized impedance from 0.619 to 0.388, corresponding to a 37.3% reduction. The largest voltage-based peak appears at 112.3 Hz, which lies in the low-order oscillation band that can excite active-power feedback ripple. By contrast, the flux-linkage case shifts the peak toward the upper end of the examined band and increases the minimum phase from 50.6° to 72.8°. These indicators show that the flux-linkage calculation weakens the modeled synchronization-loop resonance contribution and shifts the impedance response toward a more inductive characteristic.

Figure 2 presents the normalized output-impedance magnitude over 1–1000 Hz, and Table 4 reports separate 10–40, 40–250, 250–500, and 500–1000 Hz indicators. The analytical scan therefore includes, rather than omits, the sub-synchronous and lower high-frequency intervals: the two 10–40 Hz maximum impedances are both 0.074 p.u., whereas the 500–1000 Hz magnitude difference is below 1%. Because the averaged impedance scan is limited to 1 kHz and cannot resolve switching-frequency components, a dedicated closed-loop EMT analysis sampled at 50 kHz was added in Section 5.3 to examine 10–40 Hz directly and extend the high-frequency evidence to 10 kHz. The combined evidence is used to distinguish a 40–250 Hz synchronization-interaction benefit from the behavior in the two reviewer-requested bands.

The inertia-dependent denominator in (18) gives $\omega_n = \sqrt{\omega_0 K_s/J}$ and $\zeta = D/(2\sqrt{J\omega_0 K_s})$. Thus, increasing J without retuning D lowers the mode frequency and reduces the damping ratio, so excessive virtual inertia can degrade load-step and post-fault stability. This effect was quantified by time-domain integration of (13) for a 0.10 p.u. active-power step, using $E = V = 1$ p.u., $X = 0.10$ p.u., $P_0 = 0.60$ p.u., and $K_s = 9.982$. Table 5 reports the result using the nominal inertia/damping pair as the base. Raising inertia from $2J_0$ to $4J_0$ at fixed damping reduces the peak frequency deviation, but reduces ζ from 0.505 to 0.357 and almost doubles the 2% settling time; across the whole sweep, the fixed-damping ratio falls from 0.714 at J_0 to 0.357 at $4J_0$. Increasing damping proportionally to $\sqrt{J}$ restores the nominal-$2J_0$ damping ratio and improves settling. Hence, high virtual inertia is not intrinsically stabilizing or destabilizing; it must be co-tuned with damping [21, 22].

5. NUMERICAL EXPERIMENTS

5.1. PSCAD Simulation Setup

Figure 4 shows the simulated topology implemented in PSCAD 5.0.0 Professional. Each model contains three parallel VSG units (VSC1-VSC3), with active-power references of 0.6 p.u. for VSC1 and 0.5 p.u. for VSC2 and VSC3.

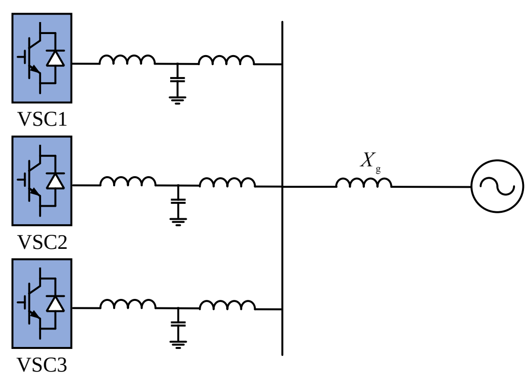

FIGURE 4. Simulated topology of the paralleled VSG system.

Table 6 summarizes simulation conditions. For each case, the same parameter change is applied to both the flux-based and voltage-based models, so the comparison isolates the influence of the active-power calculation path.

5.2. Closed-Loop Active-Reactive Power-Coupling Validation

To complement the controlled steady-state sweep in Table 2, we executed six closed-loop PSCAD/EMTDC cases: flux- and voltage-based models were each evaluated with $|Z_{\text{int}}| = 0.20$ p.u. at $R/X = 0.1$ and 1.0, together with a stronger-

TABLE 4. Extended output-impedance scan from 10 Hz to 1 kHz. The reported values are the maximum magnitude and minimum phase within each interval.

Band (Hz)	Flux max. $\lvert Z_{\text{out}}\rvert$	Voltage max. $\lvert Z_{\text{out}}\rvert$	Flux min. phase (deg.)	Voltage min. phase (deg.)
10–40	0.074	0.074	34.6	37.2
40–250	0.388	0.619	72.8	50.6
250–500	0.792	0.823	84.8	66.0
500–1000	1.596	1.611	88.1	78.5

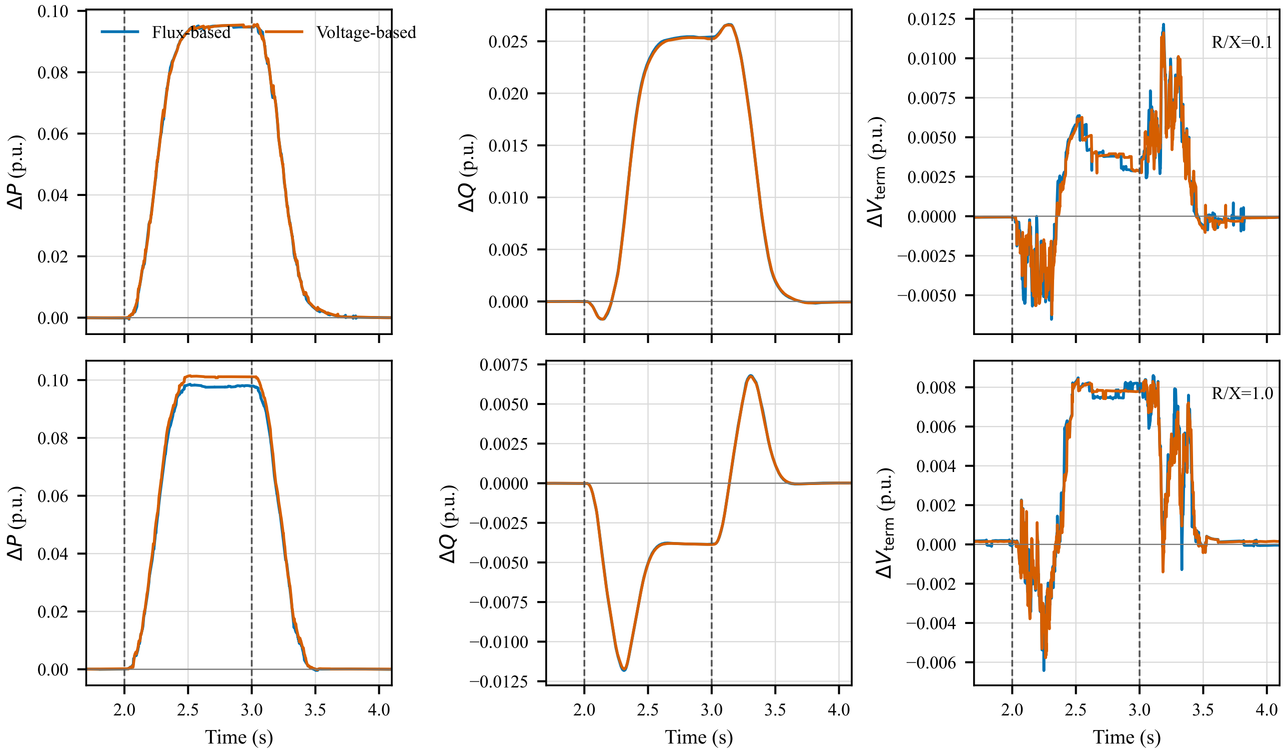

FIGURE 5. Closed-loop PSCAD/EMT response to the matched active-power reference commands for $|Z_{\text{int}}| = 0.20$ p.u. The top and bottom rows use $R/X = 0.1$ and 1.0, respectively. Curves are the three-VSC means after subtracting the 1.70–1.95 s pre-event mean; a centered moving average with a 20 ms window is used for display only. V_{term} is the local converter-terminal voltage magnitude derived from the native three-phase voltage channels, not a common-PCC measurement.

TABLE 5. Numerical swing-equation step sweep for virtual inertia and damping.

J/J_0	D/D_0	f_n (Hz)	ζ	Peak $\lvert\Delta f\rvert$ (Hz)	2% settling time(s)
1	1.000	8.913	0.714	0.0405	0.126
2	1.000	6.302	0.505	0.0343	0.233
4	1.000	4.456	0.357	0.0282	0.436
4	1.414	4.456	0.505	0.0243	0.330

interface reference at $|Z_{\text{int}}| = 0.05$ p.u. and $R/X = 0.1$. Here, Z_{int} is the identical series R-L impedance assigned to each of the three converter-grid interface branches; $R = |Z_{\text{int}}|(R/X)/\sqrt{1+(R/X)^2}$ and $X = |Z_{\text{int}}|/\sqrt{1+(R/X)^2}$. The custom delayed two-port parameters were calibrated so that the exact discrete differential-mode impedance at 50 Hz matches each target $R+\mathrm{j}X$ with a 10 µs solution step; with $R = 0$, its admittance and history-source coefficients reduce exactly to those of the original lossless component. At $t = 2.0$ s, every VSC receives the same $+0.1$ p.u. active-power reference command, which returns at $t = 3.0$ s through the existing 0.4 p.u./s reference rate limiter. Each run lasts 6.0 s with a 10 µs EMT solution step and a 250 µs output step. Native P, Q, frequency, current, and three-phase local converter-terminal-voltage channels are retained for every VSC. The analytical sweep isolates R/X at a common P-Q-V point; the EMT models retain their original regulators, so Table 7 reports resulting pre-event operating points and treats each response as a case-wise closed-loop validation rather than isolated dynamic R/X sensitivity.

Figure 5 and Table 7 show direct active-reactive coupling in both calculation methods. For $|Z_{\text{int}}| = 0.20$ p.u. and $R/X = 0.1$, the three-VSC mean steady reactive-power changes are 0.0254 and 0.0253 p.u. for the flux- and voltage-based methods, respectively. At $R/X = 1.0$, both changes reverse sign to approximately -0.0038 p.u. In the two $|Z_{\text{int}}| = 0.20$ cases, the

TABLE 6. Main PSCAD simulation settings.

Item	Setting
Converter units	Three paralleled VSG converters, denoted as VSC1, VSC2, and VSC3
Active-power references	0.6 p.u. for VSC1; 0.5 p.u. for VSC2 and VSC3
Rated frequency	50 Hz
Simulation time and step	5 s; 250 µs output sampling step
Closed-loop P-Q coupling run	Three identical converter-grid interface branches; $\lvert Z_{\text{int}}\rvert = 0.05$ or 0.20 p.u.; $R/X = 0.1$ or 1.0; 6.0 s duration; 10 µs EMT solution step; 250 µs output step
Dedicated frequency-band run	$X_{\text{g}} = 0.20$ p.u.; 3.5 s duration; 10 µs EMT solution step; 20 µs output step (50 kHz sample rate)
Balanced disturbance	Three-phase-to-ground grid fault (deep balanced voltage sag) at 2.0 s, lasting 0.3 s
Asymmetric disturbance	Phase-a-to-ground disturbance at 2.0 s, lasting 0.3 s, zero fault resistance
Extended cases	A-B fault, A-B-ground fault, balanced voltage sag to 0.8 p.u., and grid-frequency dip to 49.5 Hz under $X_{\text{g}} = 0.10$ p.u.
Grid-impedance sweep	$X_{\text{g}} = 0.05$, 0.10, and 0.20 p.u.
Operating-point sweep	$X_{\text{g}} = 0.10$ p.u.; active-power references scaled by 0.8, 1.0, and 1.2
Filter-parameter sweep	$L_f = 0.15$ mH and $C_f = 10$ µF; each varied to 0.7 and 1.3 times its nominal value

TABLE 7. Closed-loop active-reactive power-coupling metrics. The pre-event three-VSC means (P_0, Q_0, V_0) use 1.70–1.95 s; steady changes use 2.70–2.95 s minus the pre-event mean. "20 ms max" is the largest absolute cycle-averaged excursion among the three VSCs. The residual columns give the largest absolute 5.65–5.90 s return residual among the three VSCs. The strict short-horizon flag is triggered by an insufficiently decaying, sustained, or growing cycle-averaged oscillation, or by a Q/V_{term} mean residual exceeding the stated noise-scaled threshold, with a minimum residual threshold of 0.001 p.u.

$\lvert Z_{\text{int}}\rvert$, R/X	Method	(P_0, Q_0, V_0) (p.u.)	ΔP_{ss}	ΔQ_{ss}	ΔV_{ss}	20 ms max $\lvert\Delta Q\rvert$	20 ms max $\lvert\Delta V_{\text{term}}\rvert$	max $\lvert Q_{\text{res}}\rvert$	max $\lvert V_{\text{res}}\rvert$	Flag
0.20, 0.1	Flux-based	(0.4943, 0.0943, 0.9274)	0.0950	0.0254	0.0034	0.0290	0.0168	0.000023	0.000280	No
0.20, 0.1	Voltage-based	(0.5069, 0.0943, 0.9276)	0.0952	0.0253	0.0037	0.0289	0.0176	0.000031	0.000343	No
0.20, 1.0	Flux-based	(0.4923, −0.0648, 0.9259)	0.0977	−0.0038	0.0075	0.0131	0.0132	0.000035	0.000210	No
0.20, 1.0	Voltage-based	(0.5045, −0.0648, 0.9260)	0.1011	−0.0038	0.0076	0.0130	0.0132	0.000033	0.000398	No
0.05, 0.1	Flux-based	(0.4949, 0.0484, 0.9287)	0.0959	0.0177	0.0061	0.0204	0.0128	0.000026	0.000886	No
0.05, 0.1	Voltage-based	(0.5089, 0.0483, 0.9288)	0.0958	0.0177	0.0057	0.0202	0.0098	0.000033	0.001081	Yes

largest local terminal-voltage excursion averaged over 20 ms is 0.0176 p.u.; the worst 5.65–5.90 s reactive-power and local-voltage residuals are 3.5×10^{-5} and 3.98×10^{-4} p.u. All four weak-interface runs clear the short-horizon diagnostic. Across all six runs, no growing cycle-averaged Q or local-voltage oscillation is observed; only the stronger-interface voltage-based case triggers the strict flag because one VSC retains a local-voltage mean offset of 0.001081 p.u., despite a post-/early-event voltage standard-deviation ratio of 0.00123. Thus, the evidence supports bounded case-wise behavior over 6 s but not a formal stability-boundary claim. The near-coincident flux- and voltage-based responses also show that the proposed active-power calculation does not by itself decouple P and Q; explicit virtual-impedance or decoupling control remains necessary when application limits require it.

5.3. Sub-Synchronous and High-Frequency Validation

The previously unreported 10–40 Hz and > 500 Hz bands were evaluated in a dedicated pair of closed-loop PSCAD/EMT runs at $X_{\text{g}} = 0.20$ p.u. Both models used the same three-phase-

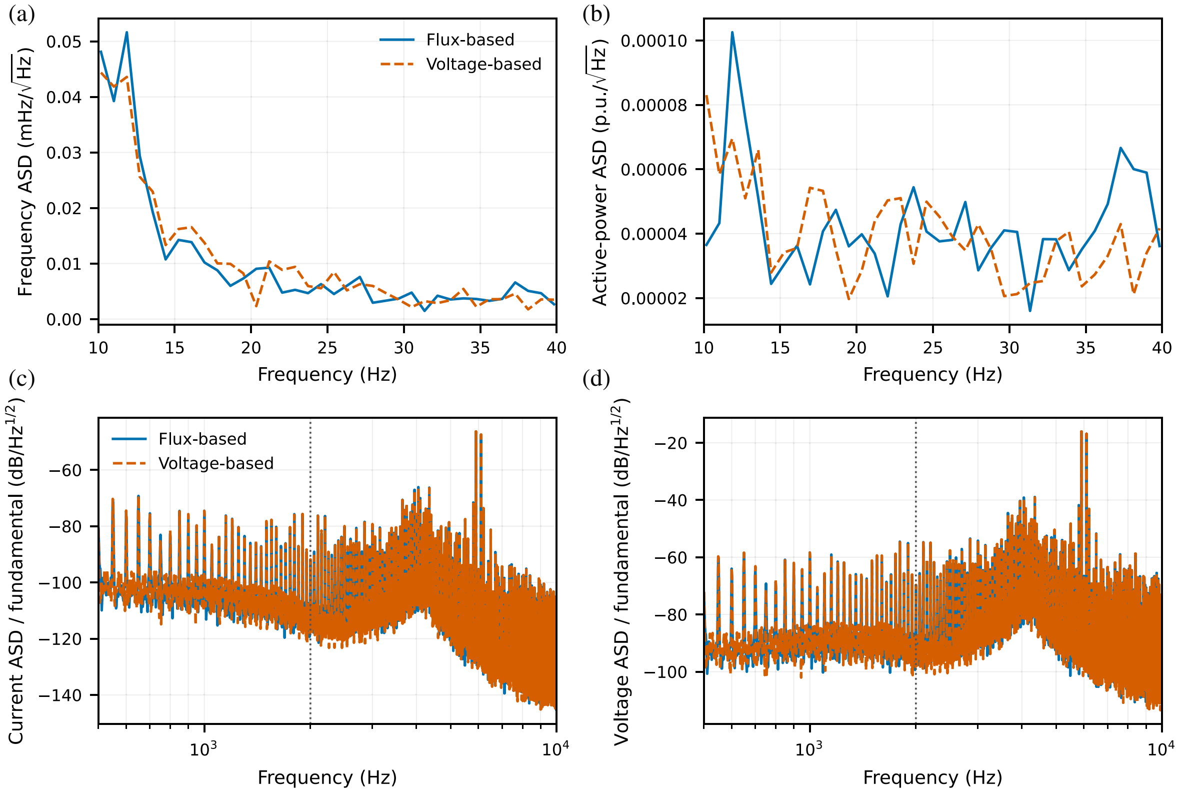

FIGURE 6. Dedicated frequency-band validation from PSCAD/EMT runs sampled at 50 kHz. (a) Frequency and (b) active-power amplitude spectral density in the 10–40 Hz post-fault recovery interval. Pre-fault (c) current and (d) voltage spectra from 500 Hz to 10 kHz are normalized by the corresponding fundamental rms. Curves are averaged across three VSCs; the dotted line separates 500–2000 Hz and 2–10 kHz reporting bands.

TABLE 8. Frequency-band metrics from the dedicated high-resolution EMT runs. Values are reported as the mean $\pm$ sample standard deviation (SD) across VSC1-VSC3 ($n = 3$). Here, F and V denote the corresponding three-VSC means for the flux- and voltage-based methods, respectively; the relative difference is $100(F - V)/V$, and a positive value means that the flux-based result is larger.

Window	Quantity (reported unit)	Band (Hz)	Flux-based	Voltage-based	Relative difference, $100(F - V)/V$ (%)
Recovery	Frequency rms (mHz)	10–40	0.0879 ± 0.0071	0.0857 ± 0.0030	$+2.64$
Recovery	Active-power rms (10^{-3} p.u.)	10–40	0.246 ± 0.050	0.234 ± 0.012	$+5.12$
Pre-fault	Current rms/fundamental (%)	500–2000	0.124 ± 0.014	0.126 ± 0.018	-1.19
Pre-fault	Current rms/fundamental (%)	2000–10000	1.080 ± 0.110	1.081 ± 0.110	-0.082
Pre-fault	Voltage rms/fundamental (%)	500–2000	0.763 ± 0.063	0.765 ± 0.084	-0.259
Pre-fault	Voltage rms/fundamental (%)	2000–10000	35.099 ± 0.075	35.098 ± 0.061	$+0.002$

to-ground fault from 2.0 to 2.3 s, a 10 µs EMT solution step, and a 20 µs output step. The resulting 50 kHz sample rate and 25 kHz Nyquist frequency resolve the 6 kHz PWM carrier and its neighboring components. The 10–40 Hz metrics use the 2.32–3.50 s post-fault recovery window. High-frequency metrics use both the 1.00–1.90 s pre-fault interval and the 2.32–3.20 s recovery interval. Hann-window periodogram was used for the low band, and phase-averaged Welch spectrum was used above 500 Hz. Table 8 reports the mean and standard deviation across all three VSCs; high-frequency band rms values are normalized by the corresponding 45–55 Hz fundamental rms.

Figures 6(a)–(b) and Table 8 show similarly small 10–40 Hz content for both methods, with no growing band component observed within the analyzed recovery window. The flux-based values are 2.64% higher for frequency and 5.12% higher for active power, so the added analysis does not support a sub-synchronous damping advantage. Above 500 Hz, the current and voltage spectra are nearly coincident. Both methods have the same dominant line at 5.901 kHz, close to the 6 kHz PWM carrier used in both models. Over the complete 500 Hz–10 kHz interval, pre-fault current values are 1.087% and 1.088% of the fundamental for flux- and voltage-based methods, respectively, and the corresponding voltage values are 35.108% and

TABLE 9. Estimator robustness from recorded-EMT waveform replay. Entries are mean active-power NRMSE (%) across three VSGs and the two saved fault cases.

Perturbation	4–5 s steady interval		2–2.3 s fault interval	
	Plain integral	Mean removed	Plain integral	Mean removed
1% dc voltage offset	182.8	13.64	216.6	1.41
0.5% zero-mean voltage noise	0.659	2.57	1.170	0.259
5% current-gain error	5.60	5.35	5.59	5.46

35.107%. During post-fault recovery, their relative differences remain below 0.5% for current and 0.2% for voltage. Thus, no method-dependent high-frequency resonance is observed or suppressed by changing the power-calculation path; those components are governed mainly by the shared PWM, inner loops, and filter. The direct analysis of both requested bands localizes the principal method-dependent attenuation to the 40–250 Hz power-feedback interaction.

5.4. Estimator Robustness under Measurement Errors

The offset/noise sensitivity derived in Section 3 was evaluated by injecting measurement errors offline into recorded PSCAD voltage/current waveforms from both three-phase-to-ground and phase-a-to-ground cases. This waveform replay tests the estimator only and does not constitute a new closed-loop EMT run. Table 9 reports the mean normalized active-power root-mean-square error (NRMSE), averaged over the three VSGs and both saved disturbances. With a 1% phase-wise dc voltage offset, mean removal reduces the NRMSE from 182.8% to 13.64% in the 4–5 s steady interval and from 216.6% to 1.41% in the 2–2.3 s fault interval. The 5% current-gain perturbation gives comparable errors for the two estimators, whereas the ten-sample mean-removal filter is less favorable for zero-mean 0.5% white voltage noise in the steady interval. These results quantify the intended dc-drift rejection and its noise trade-off; a bounded leaky integrator, a second-order generalized integrator (SOGI), or an observer-based estimator can be used when the sensor-noise spectrum is unfavorable.

5.5. Inter-Converter Synchronization and Scalability

The simulated plant contains three paralleled VSGs. Around a synchronous operating point, the electrical-power perturbation of unit i can be written in the reduced form $\Delta P_{\mathrm{e,i}} = \sum_{j\neq i} K_{ij}(\Delta\delta_i - \Delta\delta_j) + K_{E,i}\Delta E_i + \Delta P_{\mathrm{dist,i}}$. The common mode is associated with the shared bus frequency, whereas the differential modes are associated with angle differences among VSC1-VSC3. The proposed flux calculation attenuates $\Delta P_{\mathrm{dist,i}}$ before it enters each swing loop; it does not change network synchronizing coefficients K_{ij}. The recorded three-converter PSCAD data were therefore reevaluated using the normalized sharing-dispersion index $\sigma_P/|\bar{P}_{\mathrm{pre}}|$, where σ_P is the standard deviation of the three instantaneous active powers, and $\bar{P}_{\mathrm{pre}}$ is their common pre-fault mean. During the three-phase-to-ground fault, this index is 5.71% for the flux calculation and 11.74% for the voltage calculation; during the phase-a-to-ground fault, the corresponding values are 7.67% and 7.75%. Post-fault values are similar (11.47% and 11.77% in the balanced case), indicating that the flux path improves differential sharing during the severe fault without introducing a persistent post-fault sharing penalty. The result establishes compatible parallel operation for the stated three equal-rating VSGs, but it is not a proof for arbitrary converter counts, heterogeneous virtual inertias, communication delays, or mixed grid-forming/grid-following plants. Those cases require a full multi-converter impedance or state-space study, including sequence coupling [23].

Current and voltage total harmonic distortions are calculated as

$$\mathrm{THD} = \frac{\sqrt{\sum_{n=2}^{N} X_n^2}}{X_1} \times 100\%. \tag{20}$$

The active-power ripple used in this paper is

$$r_P = \frac{P_{\max} - P_{\min}}{|\bar{P}|} \times 100\%, \tag{21}$$

evaluated over the steady-state interval from 4 s to 5 s. To quantify the harmonic/oscillatory component of the VSG feedback signal, the non-dc active-power component is also calculated as

$$r_{P,\mathrm{ac}} = \frac{\mathrm{rms}(P - \bar{P})}{|\bar{P}|} \times 100\%. \tag{22}$$

This index is not a terminal-voltage or terminal-current THD. It directly measures the ac component in the active-power signal that enters the swing equation.

5.6. Dynamic Response after Grid Disturbance

Figure 7 compares active-power responses around the grid disturbance. To avoid hiding the ripple difference by plotting all curves on one axis, the flux-linkage-based and voltage-based results are shown in separate panels with the same vertical scale. Both models ride through the disturbance, but the voltage-based power signal contains much denser oscillatory excursions during and after the fault. The flux-based method gives a visibly smoother power feedback after the disturbance is cleared, reducing the oscillatory input to the swing equation.

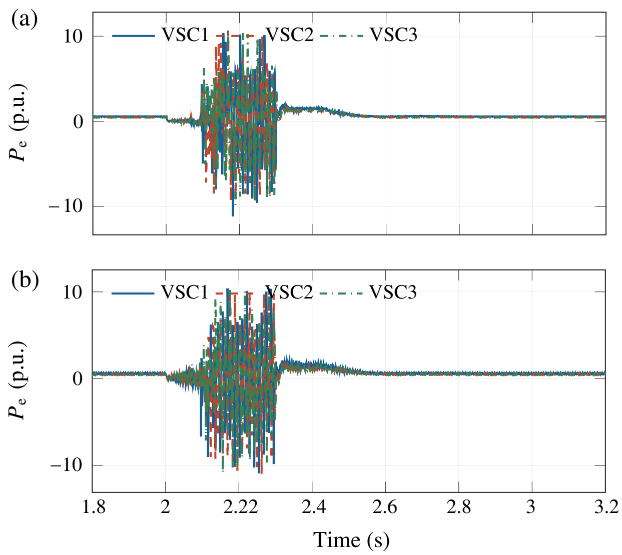

FIGURE 7. Separated active-power responses after the grid disturbance. (a) Flux-linkage-based VSG and (b) voltage-based VSG.

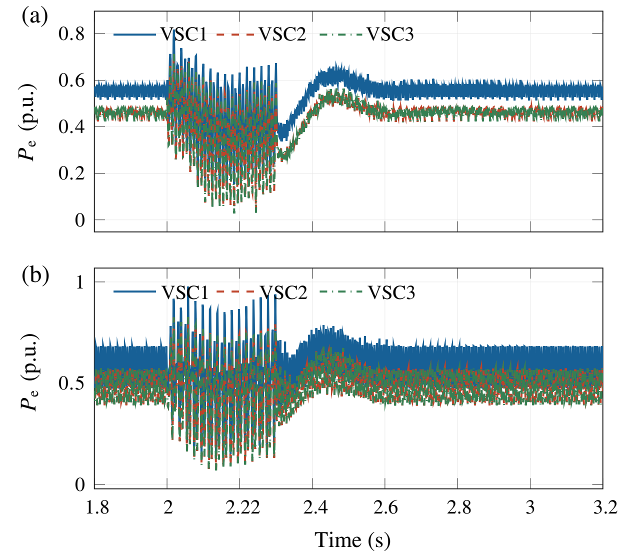

FIGURE 8. Active-power response under the phase-a-to-ground fault. (a) Flux-linkage-based VSG and (b) voltage-based VSG.

5.7. Asymmetric Disturbance Test

To further test the method under unbalanced grid conditions, an additional PSCAD case replaces the three-phase-to-ground fault with a phase-a-to-ground disturbance. The grid impedance is $X_g = 0.10$ p.u.; the fault is applied from 2.0 to 2.3 s with zero resistance. Fig. 8 shows the response. During the single-line-to-ground interval, negative-sequence quantities excite both controllers. After the fault is cleared, however, the voltage-based power calculation keeps a larger oscillatory component, whereas the flux-linkage-based calculation settles to a narrower ripple band.

The post-fault interval in Table 10 is especially relevant to the VSG synchronization loop because it represents the feedback signal that remains after the disturbance is removed. In this interval, the flux-linkage method reduces the average active-power peak-to-peak ripple by 65.8% and the active-power ac rms component by 71.4% relative to the voltage-based method. The averaged frequency peak-to-peak value is also reduced from 6.29×10^{-4} p.u. to 2.11×10^{-4} p.u. Therefore, the proposed method not only is effective for balanced disturbances and operating-point changes, but also reduces the observed post-fault power and frequency ripple under the tested unbalanced disturbance.

5.8. Additional Disturbance Validation

To add simulation evidence for reviewer-requested multi-phase faults, voltage sags, and frequency events, four closed-loop PSCAD cases were evaluated under $X_g = 0.10$ p.u.: an A-B fault, an A-B-ground fault, a balanced voltage sag to 0.8 p.u., and a grid-frequency dip to 49.5 Hz. Table 11 summarizes the fleet-averaged power, frequency, current, and voltage indicators, and Fig. 11 shows corresponding time-domain traces.

The added cases show that the flux-linkage path reduces the peak active-power deviation by 2.98%, 8.97%, 41.89%, and 24.24% for the A-B fault, A-B-ground fault, voltage sag to

TABLE 10. Active-power feedback oscillation under the phase-a-to-ground fault.

Window	Method	P ripple (%)	$P_{ac,rms}$ (%)
2.3–3.2 s	Flux	71.52	10.32
2.3–3.2 s	Voltage	81.44	14.08
4.0–5.0 s	Flux	15.31	3.60
4.0–5.0 s	Voltage	44.76	12.57

0.8 p.u., and grid-frequency dip to 49.5 Hz, respectively. It also reduces recovery power RMS in all four cases, whereas the event-window RMS and frequency-deviation indicators remain disturbance-dependent. Together, these results extend the evidence to additional disturbance types and confirm the benefit of conditioning the active-power feedback that enters the VSG swing loop.

5.9. Steady-State Waveform and Harmonic Characteristics

Fig. 9 and Fig. 10 show terminal phase-a current and voltage waveforms. The two methods produce almost overlapping terminal waveforms because the converter topology, filter, grid parameters, and voltage/current inner loops are the same. The comparable terminal-waveform quality, together with the reduced power ripple reported above, localizes the observed improvement to the active-power feedback quantity used by the VSG synchronization loop.

5.10. Weak-Grid Ripple Suppression

Table 12 shows that terminal current and voltage THD values are almost the same for the two methods. In contrast, the active-power ripple is much smaller with the flux-linkage-based calculation. As shown in Fig. 12, the flux-based method keeps the average active-power ripple below 20% for all tested impedances, whereas the voltage-based method remains above 43%.

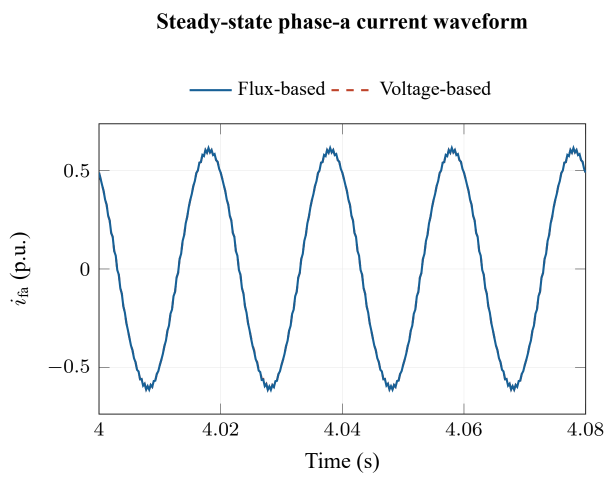

FIGURE 9. Steady-state phase-a current waveform in the base case.

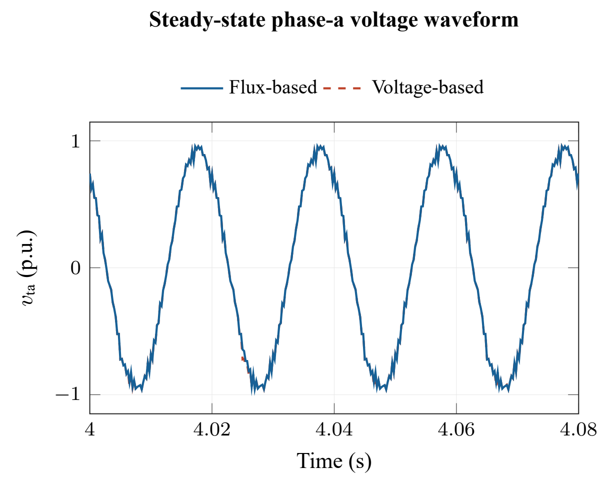

FIGURE 10. Steady-state phase-a voltage waveform in the base case.

TABLE 11. PSCAD validation under additional multi-phase faults and grid disturbances ($X_{\text{g}} = 0.10$ p.u.)

Scenario	Method	max $\lvert\Delta P\rvert$ (p.u.)	P-RMS (event) (p.u.)	P-RMS (recovery) (p.u.)	max $\lvert\Delta f\rvert$ (Hz)	I_{pk} (p.u.)	$V_{\min}/V_0$ (p.u.)
A-B fault	Flux-based	1.771	0.935	0.180	0.289	2.278	0.226
	Voltage-based	1.826	0.807	0.260	0.322	2.602	0.225
A-B-ground fault	Flux-based	1.638	0.809	0.166	0.252	2.353	0.257
	Voltage-based	1.800	0.754	0.235	0.285	2.534	0.257
Voltage sag to 0.8 p.u.	Flux-based	0.198	0.070	0.064	0.091	0.843	0.736
	Voltage-based	0.341	0.096	0.109	0.087	0.844	0.734
Frequency dip to 49.5 Hz	Flux-based	0.858	0.656	0.176	0.504	1.394	0.806
	Voltage-based	1.132	0.711	0.215	0.497	1.406	0.807

TABLE 12. Average steady-state performance under different grid impedances.

X_{g}	Method	I_{THD} (%)	V_{THD} (%)	P ripple (%)	Δf (p.u.)
0.05	Flux	1.561	4.494	19.04	0.000378
0.05	Voltage	1.565	4.496	43.98	0.000659
0.10	Flux	1.364	4.461	15.29	0.000222
0.10	Voltage	1.362	4.436	44.74	0.000667
0.20	Flux	1.075	4.122	16.45	0.000303
0.20	Voltage	1.086	4.217	44.14	0.000622

Fig. 13 shows the frequency ripple trend. Since the VSG swing equation is driven by active-power feedback, the cleaner flux-based power signal reduces frequency oscillation. The frequency peak-to-peak value is reduced by 42.6% in the base case and by more than 51% in the weak-grid cases.

Reduction factors in Table 13 quantify this separation between terminal harmonic performance and synchronization-loop ripple attenuation. The strongest grid case still gives a 56.7% reduction in active-power ripple, while the two weaker-grid cases keep the reduction above 62%. The frequency-ripple reduction follows the same trend, indicating that the

TABLE 13. Reduction obtained by the flux-based power calculation relative to the voltage-based calculation.

X_{g}	P ripple reduction (%)	Frequency ripple reduction (%)
0.05	56.7	42.6
0.10	65.8	66.7
0.20	62.7	51.3

flux-linkage calculation mainly improves the quality of the VSG feedback variable rather than changing the physical voltage/current filtering path.

The operating-point sweep in Table 14 and Fig. 14 further shows the active-power feedback-ripple advantage. Under $X_{\text{g}} = 0.10$ p.u., changing the power reference to 0.8 and 1.2 times the nominal value does not change the conclusion: the flux-linkage calculation keeps $P_{\text{ac,rms}}$ around 3.5–3.8%, while the conventional voltage-based calculation remains around 12.5–12.8%. In other words, the flux-linkage method reduces the non-dc active-power feedback component by 69.9–72.7%. Fig. 15 gives a time-domain example for the heavy-power weak-grid case, where the voltage-based power feedback contains larger steady oscillations even though the terminal voltage/current waveforms remain similar.

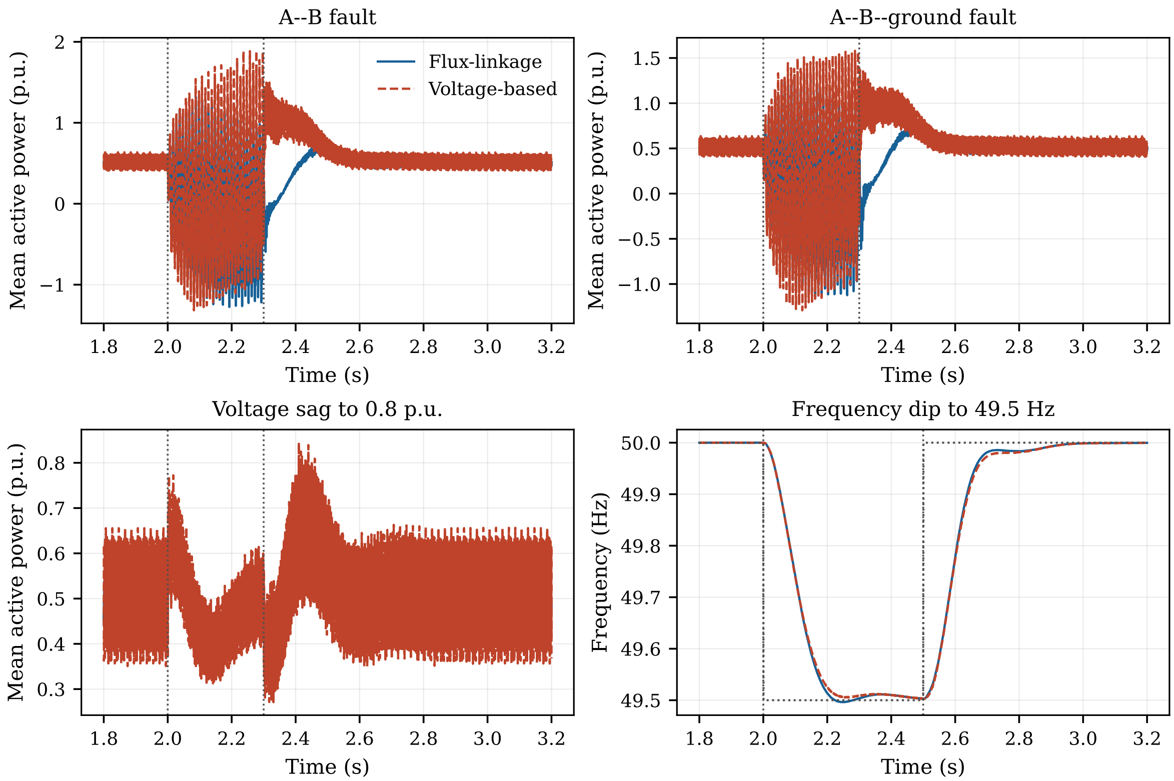

FIGURE 11. Closed-loop PSCAD responses under the additional multi-phase fault, voltage-sag, and grid-frequency-dip validation cases.

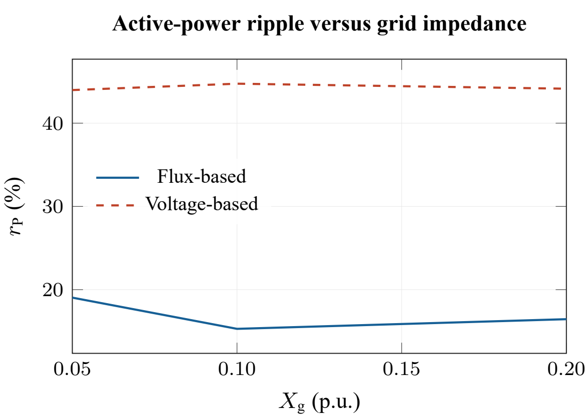

FIGURE 12. Active-power ripple under different grid impedances.

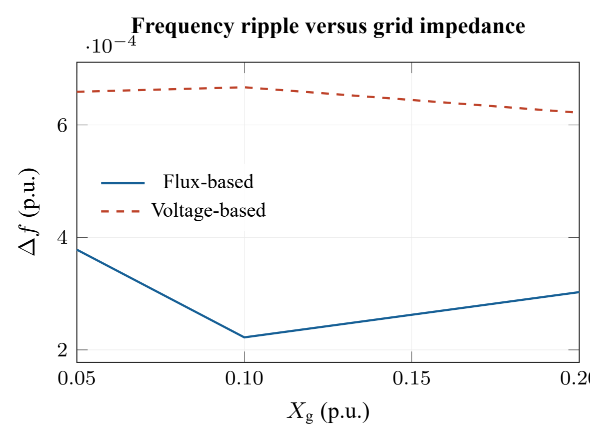

FIGURE 13. Frequency ripple under different grid impedances.

5.11. Filter-Parameter Sensitivity

The sensitivity to filter parameters is further examined under the weak-grid condition $X_g = 0.10\,\text{p.u.}$ The physical inverter-side filter inductor and shunt filter capacitor are varied separately by $\pm 30\%$ from their nominal values, namely $L_f = 0.15\,\text{mH}$ and $C_f = 10\,\mu\text{F}$. The voltage and current inner-loop gains are not retuned, so this test reflects the robustness to plant-parameter deviation rather than an optimized redesign for each filter.

Table 15 shows that the terminal current and voltage THD are almost identical for the two methods under the same filter perturbation. This is expected because the power-calculation block does not change the physical filter. Reducing L_f or C_f substantially increases the terminal-voltage THD for both methods, whereas increasing the filter parameter reduces the terminal harmonic content.

The active-power feedback and frequency responses show different sensitivities. As shown in Fig. 16, the flux-linkage method keeps the lower $P_{ac,rms}$ value for the nominal and enlarged-filter cases, whereas reducing L_f or C_f by 30% increases its raw active-power feedback component. Fig. 17 shows lower frequency peak-to-peak values for the nominal case, both reduced-filter cases and the enlarged-L_f case; only the enlarged-C_f case gives a slightly larger value for the flux-linkage method. Thus, the most consistent benefit across this sweep is lower synchronization-frequency ripple in four of the five tested cases, while terminal THD remains governed by the physical filter and raw active-power ripple depends on the direction of the parameter deviation.

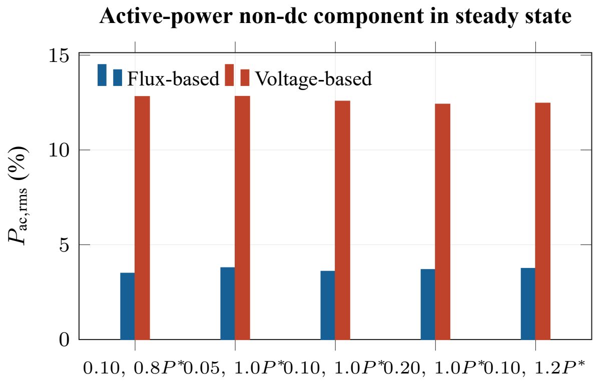

FIGURE 14. Non-dc component of the active-power feedback under different operating points.

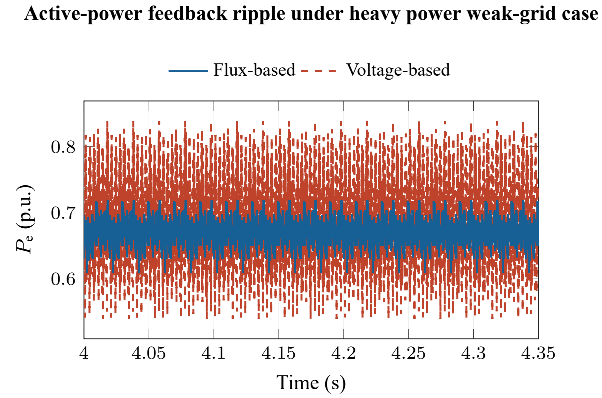

FIGURE 15. Steady-state active-power feedback ripple under the heavy-power weak-grid case.

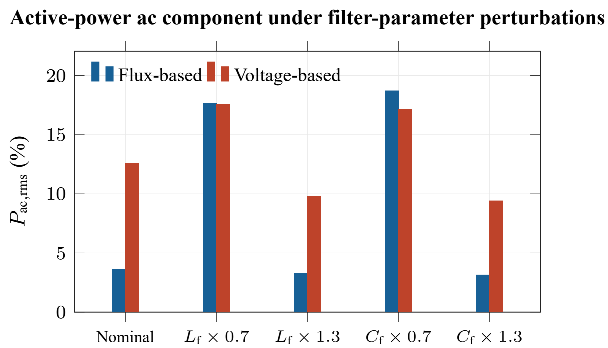

FIGURE 16. Active-power ac component under filter-parameter perturbations.

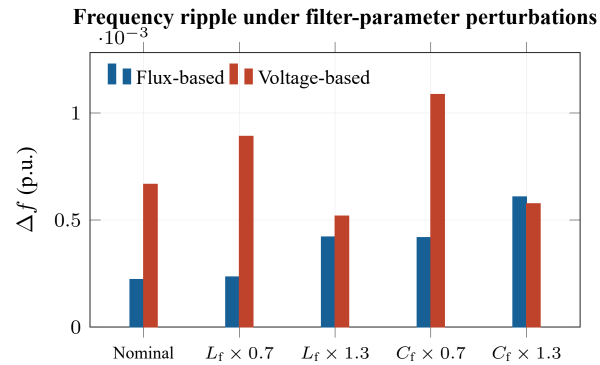

FIGURE 17. Frequency ripple under filter-parameter perturbations.

TABLE 14. Operating-point comparison of active-power oscillatory content.

(X_g, P^*)	Method	P ripple (%)	$P_{\mathrm{ac,rms}}$ (%)	Δf (p.u.)
0.10, 0.8	Flux	15.48	3.49	0.000398
0.10, 0.8	Voltage	44.31	12.81	0.000527
0.05, 1.0	Flux	19.04	3.79	0.000378
0.05, 1.0	Voltage	43.98	12.82	0.000659
0.10, 1.0	Flux	15.29	3.60	0.000222
0.10, 1.0	Voltage	44.74	12.57	0.000667
0.20, 1.0	Flux	16.45	3.69	0.000303
0.20, 1.0	Voltage	44.14	12.41	0.000622
0.10, 1.2	Flux	16.49	3.75	0.000358
0.10, 1.2	Voltage	45.16	12.46	0.000742

5.12. Discussion

The small-signal model and EMT simulations consistently identify the active-power feedback path as the source of the observed improvement. With identical voltage and current inner loops, the flux-linkage-based path reduces the peak normalized impedance in the 40–250 Hz interaction band from 0.619 to 0.388 and produces lower active-power and frequency ripple across the tested grid impedances, operating points, balanced and unbalanced disturbances, and most filter-parameter cases. This agreement links the impedance-domain mechanism to the smoother time-domain synchronization response.

The band-resolved studies define the scope of this improvement. The two calculation methods exhibit comparable 10–40 Hz post-fault content and nearly coincident current and voltage spectra from 500 Hz to 10 kHz. The demonstrated attenuation is therefore associated with the 40–250 Hz synchronization interaction rather than with broadband damping or high-frequency harmonic suppression. The analytical and closed-loop active-power-command cases also show that both methods retain the physical P-Q coupling determined by grid impedance and operating conditions. The tested responses remain bounded over observation windows of 6 s, although one stronger-interface voltage-based case retains a local-voltage mean offset of 0.001081 p.u. Accordingly, the present evidence establishes case-wise dynamic behavior but does not constitute a global stability-boundary proof. Terminal harmonic sensitivity and fault-current demand remain governed primarily by the physical filter, inner-loop design, and current-limiting strategy.

The fault cases comprise a three-phase-to-ground deep voltage sag and a phase-a-to-ground fault. The recorded waveforms were additionally replayed offline through a representative $I_{\max} = 1.2$ p.u. vector-current supervisor to quantify the limiting requirement. In the three-phase-to-ground case, the unconstrained current magnitude reaches 2.929 p.u. for the flux calculation and 2.932 p.u. for the voltage calculation, and re-

TABLE 15. Filter-parameter sensitivity under $X_{\mathrm{g}} = 0.10$ p.u.

Filter case	Method	P ripple (%)	$P_{\mathrm{ac,rms}}$ (%)	Δf (p.u.)	$I_{\mathrm{THD}}/V_{\mathrm{THD}}$ (%)
Nominal	Flux	15.29	3.60	0.000222	1.364/4.461
Nominal	Voltage	44.74	12.57	0.000667	1.362/4.436
$L_{\mathrm{f}} \times 0.7$	Flux	63.72	17.64	0.000234	2.730/19.135
$L_{\mathrm{f}} \times 0.7$	Voltage	62.96	17.54	0.000891	2.735/19.107
$L_{\mathrm{f}} \times 1.3$	Flux	19.44	3.25	0.000421	0.955/3.559
$L_{\mathrm{f}} \times 1.3$	Voltage	32.60	9.78	0.000519	0.977/3.848
$C_{\mathrm{f}} \times 0.7$	Flux	67.69	18.69	0.000418	2.740/19.782
$C_{\mathrm{f}} \times 0.7$	Voltage	63.41	17.13	0.001087	2.746/19.751
$C_{\mathrm{f}} \times 1.3$	Flux	16.26	3.12	0.000608	0.955/3.732
$C_{\mathrm{f}} \times 1.3$	Voltage	33.57	9.39	0.000576	0.958/3.825

mains above 1.2 p.u. for 99.61% of the fault interval. The vector supervisor consequently applies mean current-scale factors of 0.461 and 0.460, retaining 47.15% and 45.07% of the respective active power. In the phase-a-to-ground case, the peak currents are 1.123 and 1.130 p.u.; thus, the limiter is inactive. These values establish the current demand and the power-curtailment consequence, but they are an offline waveform replay rather than a new closed-loop limiter simulation.

A deployable implementation should combine this vector constraint with anti-windup and reactive-current priority, for example

$$i^*_{q,\mathrm{lim}} = \mathrm{sat}(i^*_q, -I_{\max}, I_{\max}),$$

$$i^*_{d,\mathrm{lim}} = \mathrm{sgn}(i^*_d)\min\{|i^*_d|, \sqrt{I^2_{\max} - (i^*_{q,\mathrm{lim}})^2}\}.$$

Such a limiter can alter both active-reactive coupling and post-fault synchronization, and therefore must be co-designed with VSG loops [21, 24]. The additional closed-loop EMT cases above cover line-to-line, line-to-line-to-ground, voltage-sag, and commanded grid-frequency-dip disturbances, but they do not replace hardware-in-loop (HIL) or experimental prototype validation. Real-time implementation, heterogeneous converter fleets, communication delays, and hardware current-limit dynamics remain outside the present evidence set.

6. CONCLUSION

This paper has developed a flux-linkage-based active-power calculation for VSG-controlled wind-turbine converters and incorporated it into a cascaded voltage-current control structure. The derived impedance model identifies a reduction in the 40–250 Hz converter-grid interaction, while the PSCAD/EMTDC results show reductions of 56.7–65.8% in active-power feedback ripple and 42.6–66.7% in frequency ripple across the tested grid impedances. Across operating-point cases, the non-dc active-power component is reduced by 69.9–72.7%. Under the phase-a-to-ground fault, the post-fault active-power ripple decreases from 44.76% to 15.31%. The frequency-resolved studies further characterize 10–40 Hz and 500 Hz–10 kHz responses and locate the principal method-dependent improvement in the 40–250 Hz synchronization band.

Analytical and closed-loop P-Q studies quantify the dependence of reactive-power and terminal-voltage responses on grid R/X ratio and operating condition, and all tested simulations of 6 s remain bounded. Additional line-to-line, line-to-line-to-ground, voltage-sag, and grid-frequency-dip simulations support reducing oscillatory active-power feedback under a wider range of disturbances. The inertia sweep and current-limit replay further clarify the coordinated damping and protection requirements. Overall, the proposed calculation provides a practical means of improving active-power feedback quality and synchronization behavior without changing the established cascaded VSG control architecture.

ACKNOWLEDGEMENT

This study is supported by the State Key Laboratory of Advanced Power Transmission Technology (Grant No. ZY80-25-002).

REFERENCES

[1] Rosso, R., X. Wang, M. Liserre, X. Lu, and S. Engelken, "Grid-forming converters: Control approaches, grid-synchronization, and future trends — A review," *IEEE Open Journal of Industry Applications*, Vol. 2, 93–109, Apr. 2021.

[2] Teng, Y., W. Deng, W. Pei, Y. Li, L. Dingv, and H. Ye, "Review on grid-forming converter control methods in high-proportion renewable energy power systems," *Global Energy Interconnection*, Vol. 5, No. 3, 328–342, Jun. 2022.

[3] Tarimer, I. and E. O. Yuzer, "Designing of a permanent magnet and directly driven synchronous generator for low speed turbines," *Elektronika Ir Elektrotechnika*, Vol. 112, No. 6, 15–18, 2011.

[4] Guerrero, J. M., J. Matas, L. G. D. Vicuna, M. Castilla, and J. Miret, "Decentralized control for parallel operation of distributed generation inverters using resistive output impedance," *IEEE Transactions on Industrial Electronics*, Vol. 54, No. 2, 994–1004, Apr. 2007.

[5] Rocabert, J., A. Luna, F. Blaabjerg, and P. Rodríguez, "Control of power converters in AC microgrids," *IEEE Transactions on*

Power Electronics, Vol. 27, No. 11, 4734–4749, Nov. 2012.

[6] Zhang, L., L. Harnefors, and H.-P. Nee, "Power-synchronization control of grid-connected voltage-source converters," *IEEE Transactions on Power Systems*, Vol. 25, No. 2, 809–820, May 2010.

[7] Liu, Y., X. Zhou, and S. Ouyang, "Capacitor voltage synchronising control-based VSG scheme for inertial and primary frequency responses of Type-4 WTGs," *IET Generation, Transmission & Distribution*, Vol. 12, No. 14, 3461–3469, Aug. 2018.

[8] Beck, H.-P. and R. Hesse, "Virtual synchronous machine," in *2007 9th International Conference on Electrical Power Quality and Utilisation*, 1–6, Barcelona, Spain, Oct. 2007.

[9] Driesen, J. and K. Visscher, "Virtual synchronous generators," in *2008 IEEE Power and Energy Society General Meeting — Conversion and Delivery of Electrical Energy in the 21st Century*, 1–3, Pittsburgh, PA, USA, Jul. 2008.

[10] Zhong, Q.-C. and G. Weiss, "Synchronverters: Inverters that mimic synchronous generators," *IEEE Transactions on Industrial Electronics*, Vol. 58, No. 4, 1259–1267, Apr. 2011.

[11] D'Arco, S., J. A. Suul, and O. B. Fosso, "Small-signal modeling and parametric sensitivity of a virtual synchronous machine in islanded operation," *International Journal of Electrical Power & Energy Systems*, Vol. 72, 3–15, Nov. 2015.

[12] Zhou, Z., S. Pugliese, and M. Liserre, "Stability comparison of grid-forming converters with different power calculation strategies," in *2023 IEEE 14th International Symposium on Power Electronics for Distributed Generation Systems (PEDG)*, 800–805, Shanghai, China, Jun. 2023.

[13] Leon, J. D. V., A. Tarraso, J. I. Candela, J. Rocabert, and P. Rodriguez, "Grid-forming controller based on virtual admittance for power converters working in weak grids," *IEEE Journal of Emerging and Selected Topics in Industrial Electronics*, Vol. 4, No. 3, 791–801, Feb. 2023.

[14] Johnson, B. B., M. Sinha, N. G. Ainsworth, F. Dörfler, and S. V. Dhople, "Synthesizing virtual oscillators to control islanded inverters," *IEEE Transactions on Power Electronics*, Vol. 31, No. 8, 6002–6015, Aug. 2016.

[15] Seo, G.-S., M. Colombino, I. Subotic, B. Johnson, D. Groß, and F. Dörfler, "Dispatchable virtual oscillator control for decentralized inverter-dominated power systems: Analysis and experiments," in *2019 IEEE Applied Power Electronics Conference and Exposition (APEC)*, 561–566, Anaheim, CA, USA, Mar. 2019.

[16] Kisinga, D. A. and P. Trodden, "Virtual power circle based PQ decoupling technique for a virtual synchronous generator connected to a weak grid," in *2023 IEEE Belgrade PowerTech*, 1–6, Belgrade, Serbia, Jun. 2023.

[17] Gholami-Khesht, H., M. Monfared, and S. Golestan, "Low computational burden grid voltage estimation for grid connected voltage source converter-based power applications," *IET Power Electronics*, Vol. 8, No. 5, 656–664, May 2015.

[18] Sun, J., "Impedance-based stability criterion for grid-connected inverters," *IEEE Transactions on Power Electronics*, Vol. 26, No. 11, 3075–3078, Nov. 2011.

[19] Harnefors, L., M. Bongiorno, and S. Lundberg, "Input-admittance calculation and shaping for controlled voltage-source converters," *IEEE Transactions on Industrial Electronics*, Vol. 54, No. 6, 3323–3334, Dec. 2007.

[20] Wen, B., D. Boroyevich, R. Burgos, P. Mattavelli, and Z. Shen, "Analysis of D-Q small-signal impedance of grid-tied inverters," *IEEE Transactions on Power Electronics*, Vol. 31, No. 1, 675–687, Jan. 2016.

[21] Chen, J., Q. Gong, Y. Zhang, M. Fawad, S. Wang, C. Li, and J. Liang, "Comprehensive assessment of transient stability for grid-forming converters considering current limitations, inertia and damping effects," *CSEE Journal of Power and Energy Systems*, Vol. 11, No. 1, 1–12, Jan. 2025.

[22] Wang, J. and K. Ma, "Inertia and grid impedance emulation of power grid for stability test of grid-forming converter," *IEEE Transactions on Power Electronics*, Vol. 38, No. 2, 2469–2480, Feb. 2023.

[23] Elshenawy, M. A., A. A. A. Radwan, and Y. A.-R. I. Mohamed, "Analysis and weakening of sequence impedance coupling in grid-forming converters," *IEEE Transactions on Power Delivery*, Vol. 39, No. 6, 3292–3304, Dec. 2024.

[24] Wang, K., Q. Song, W. Liu, B. Zhao, and P. Zhang, "Reactive power characteristics and FRT strategy for grid-forming converters with virtual impedance-based current limiting," *IEEE Transactions on Energy Conversion*, Vol. 40, No. 2, 1165–1177, Jun. 2025.